



THE UNIVERSITY *of* EDINBURGH

Edinburgh Research Explorer

## Imaging for a Forward Scanning Automotive Synthetic Aperture Radar

**Citation for published version:**

Gishkori, S, Daniel, L, Gashinova, M & Mulgrew, B 2019, 'Imaging for a Forward Scanning Automotive Synthetic Aperture Radar', *IEEE Transactions on Aerospace and Electronic Systems*, vol. 55, no. 3, pp. 1420 - 1434. <https://doi.org/10.1109/TAES.2018.2871436>

**Digital Object Identifier (DOI):**

[10.1109/TAES.2018.2871436](https://doi.org/10.1109/TAES.2018.2871436)

**Link:**

[Link to publication record in Edinburgh Research Explorer](#)

**Document Version:**

Peer reviewed version

**Published In:**

IEEE Transactions on Aerospace and Electronic Systems

**General rights**

Copyright for the publications made accessible via the Edinburgh Research Explorer is retained by the author(s) and / or other copyright owners and it is a condition of accessing these publications that users recognise and abide by the legal requirements associated with these rights.

**Take down policy**

The University of Edinburgh has made every reasonable effort to ensure that Edinburgh Research Explorer content complies with UK legislation. If you believe that the public display of this file breaches copyright please contact [openaccess@ed.ac.uk](mailto:openaccess@ed.ac.uk) providing details, and we will remove access to the work immediately and investigate your claim.



# Imaging for a Forward Scanning Automotive Synthetic Aperture Radar

Shahzad Gishkori, Liam Daniel, Marina Gashinova and Bernard Mulgrew

**Abstract**—In this paper, we propose a forward scanning synthetic aperture radar methodology for a forward-looking automotive (low-terahertz) radar which combines scene scanning with synthetic aperture processing, resulting in enhanced angular resolution and improved imaging. We propose two algorithms: *i*) a modified back-projection algorithm, and *ii*) a compressed sensing based back-projection algorithm. We suggest techniques to reduce computational complexity of the proposed algorithms. Results of simulation and real-data experiments corroborate the validity of our proposed methodology and algorithms.

**Index Terms**—Automotive SAR, forward-looking SAR, terahertz, angular resolution, back-projection, compressed sensing.

## I. INTRODUCTION

Automotive (Auto-) radar has received a lot of attention over the past few years especially in the context of advanced driver assistance systems (ADASs) and highly automated driving (HAD) [1]–[3]. The main role of an Auto-radar in these applications has been restricted to detection and/or collision avoidance only, whereas scene imaging has mostly been performed by optical sensors, e.g., lidar and camera. Imaging capability of the optical sensors is substantially reduced in severe weather conditions, e.g., fog, rain, snow, etc. However, the radar can provide substantial sensing capabilities even in such harsh weather conditions, especially when operating at very high frequencies, and it can create an image of the scene for both on- and off-road driving. Therefore, we are primarily concerned with the imaging scenarios where radar is the only available sensor and all useful information, e.g., detection, classification, height estimation, etc, needs to be extracted from the radar image. Recently, automotive-terrain imaging capabilities of a low-THz (150 GHz) radar were presented in [4] by using frequency modulated continuous wave (FMCW) signalling. Low-THz frequencies provide the radar with enhanced penetration capabilities and as a result, the radar can cope with severe weather conditions. However, imaging is limited to short ranges, which is not problematic for automotive driving as the maximum imaging requirement is limited to a fraction of a kilometre only [5]. One major

challenge for the Auto-radar imaging is its range and angular resolution, especially when the targets start manoeuvring (e.g., changing lanes, etc) at short ranges (0.15 – 30 m) [5], [6]. Range resolution is primarily a function of transmit signal bandwidth, which can be increased to acquire desired results. At low-THz, signal bandwidth is of the order of tens of GHz, which can easily provide range resolution of a few centimetres. However, angular/azimuth resolution (AR) is a function of the physical aperture size of the radar antenna. Physical aperture size is generally limited by the physical constraints and cannot be changed arbitrarily. One way to circumvent this problem is to use a synthetic aperture, i.e., the radar illuminates a target scene at multiple locations and the returns are integrated coherently to generate a long synthetic aperture. This functionality gives rise to the term synthetic aperture radar (SAR). Given the movement of the vehicle, SAR processing comes natural to the Auto-radar. Generally, a side looking SAR (SL-SAR), i.e., when the axis of radar view is normal to the axis of radar motion, provides maximum gains of the synthetic aperture. However, a reduction in this normality causes a reduction in the effective synthetic aperture. An Auto-radar, in most part of its functionality, is a forward looking radar (FL-SAR), i.e., with a high squint angle, instead of a side looking radar. This causes a reduction in the effective synthetic aperture. Thus, AR enhancement of an Auto-radar with SAR mechanism has very limited gains. This paper tackles the issue of AR enhancement in this particular scenario.

**Prior Works.** A lot of work has been done in the past to enhance AR of FL-SAR. In [7], a sector imaging radar for enhanced vision (SIREV) has been presented. It is a bistatic radar with a single transmit antenna and an array of receive-only antennas. Given the absence of motion between the sensor and the targets, SAR functionality is emulated by sequentially switching between the receive antenna elements in combination with digital beamforming. However, AR is still limited by the length of the receive antenna array. Some direction of arrival (DOA) based approaches, e.g., [8]–[10], can also improve AR. However, these approaches generally require a priori knowledge of the number of scatterers to be resolved within an antenna beamwidth and/or their performance can be limited by the number of available frequency channels. A large body of literature consists of deconvolution approaches to improve the AR. Since the signal received in the angular domain, for a given range bin, can be considered (under certain assumptions) as a convolution between the antenna pattern and the targets' reflectivity pattern [11], a deconvolution process should improve the AR, in principle. In [12], an iterative noncoherent AR improvement technique has been proposed.

S. Gishkori and B. Mulgrew are with Institute for Digital Communications (IDCOM), The School of Engineering, The University of Edinburgh, United Kingdom. Emails: {s.gishkori, bernie.mulgrew}@ed.ac.uk

L. Daniel and M. Gashinova are with Microwave Integrated System Laboratory (MISL), School of Electronic, Electrical and Systems Engineering, University of Birmingham, United Kingdom. Emails: {l.y.daniel, m.s.gashinova}@bham.ac.uk

This work was supported by Jaguar Land Rover and the UK-EPSCRC grants EP/N012240/1 & EP/N012372/1 as part of the jointly funded Towards Autonomy: Smart and Connected Control (TASCC) Programme.

Processing is done in the frequency domain by approximating the inverse filter as a geometric series to avoid infinite gain at higher frequencies. However, due to noncoherent processing, the phase information is lost. In [13], a minimum mean square error (MMSE) approach was used to provide adaptive pulse compression resulting in improved range resolution. The same approach was used in [14] to propose a linear minimum mean square error (LMMSE) based method for improving AR. The AR is improved in comparison to the matched filter (MF) approach. However, the achieved AR is still comparable to the antenna pattern beamwidth. In [15], a maximum a posteriori (MAP) based approach has been proposed to improve the AR. A limiting factor for this method is the assumption of Poisson distribution of the targets' reflectivity/scattering. In [16], a truncated singular value decomposition (TSVD) based approach has been presented to enhance the spatial resolution. This approach was applied to FL-SAR in [17]. However, the key limitation in this approach is the truncation parameter which needs to be learnt.

AR improvement through deconvolution is inherently an ill-posed inverse problem, i.e., the number of unknowns (i.e., angular bins to be resolved) can be much larger than the number of available measurements. This is also referred to as an under-determined problem. The ill-posed nature of the problem can be circumvented by using certain regularization techniques. This can also result in enhancing certain features of the target scene, e.g., sparsity, grouping of the targets and non-negative nature of their reflectivities, etc. In general, the problem is formed as a least squares (LS) minimization problem regularized by various constraints. A common regularization technique, with connotations to the Wiener filter, is Tikhonov regularization which penalizes the LS cost function with an  $\ell_2$ -norm penalty. This can result in a unique solution to the problem. However, this method is devoid of sparsity. Replacing the  $\ell_2$ -norm penalty with an  $\ell_1$ -norm penalty can offer a sparse solution. This observation forms a key component of a recently introduced technique of compressed sensing (CS) [18], [19], as a solution to the under-determined problem. CS has been used in the radar related problems in a number of papers, either to create sparsity or to improve resolution (azimuth/range) or to reduce speckle, etc. (see, e.g., [20]–[22] and references therein). In [23], CS was used to improve the AR of a scanning phased array radar. AR improvement is achieved by oversampling the antenna pattern and by solving the resulting under-determined system by CS. Constraints on the measurement process are satisfied by limiting the number of targets in the scanned scene. In this paper, we use a similar approach to increase AR of an Auto-radar for a given range bin. However, our method includes SAR processing as well, which has the ability to enhance AR even further. In terms of SAR processing, a number of classical algorithms are available, e.g., Doppler beam sharpening (DBS), range migration algorithm (RMA) [11], back-projection (BP) [24], and their variants. Except for BP, most of these techniques have their limitations and can perform only under certain conditions. BP algorithm, on the other hand, is quite flexible and it can accommodate a variety of imaging scenarios. However, a limiting factor for BP

algorithm is its computational complexity. Nonetheless, some fast implementations of BP are also available, as explained in subsequent sections.

**Our Contributions.** In this paper, we provide signal processing techniques to enhance AR of the Auto-radar with the aim of forming a 2-D radar image. We use a monostatic FMCW radar working at low-THz frequencies. The radar scans the target scene at multiple look angles and then moves forward to the next scanning position/step over the aperture. We call this process as forward scanning SAR (FS-SAR). Note that steering the radar beam at multiple look angles can be done mechanically as well electronically. For the ease of explanation, we assume here a mechanically steered beam. We develop algorithms for the FS-SAR mode and verify their effectiveness via simulation as well as real-data experiments in controlled laboratory conditions. Note, on-the-road experiments are out of the scope of this paper since the main objective here is to introduce novel techniques to provide AR enhancement for Auto-radar imaging. The salient features of our paper can be detailed as below.

- 1) We propose an FS-SAR methodology as a new mode of SAR operation. We use Auto-radar as our primary application. However, the FS-SAR methodology can be extended to other forward looking scenarios.
- 2) We present a mathematical analysis for the composite antenna pattern generated by FS-SAR. We show that FS-SAR methodology causes an improvement in the effective aperture and an increase in the composite antenna gain. This results in the enhancement of AR.
- 3) We present two algorithms for the FS-SAR mode, i.e., a modified back-projection algorithm, and a compressed sensing based back-projection algorithm. The modified back-projection algorithm jointly utilizes the radar returns from all the angles and all the aperture positions. This algorithm can work directly on the radar returns and does not necessarily require any pre-processing. The compressed sensing based back-projection algorithm enhances AR by reconstructing an individual scan followed by SAR processing over the reconstructed returns of all the scans. This algorithm capitalises on the sparsity of the scene and it has the ability to reconstruct extended targets in the radar image.
- 4) We show that the computational complexity of the proposed algorithms is not a bottleneck for their practical implementation and it can be easily managed by using the already available techniques on complexity reduction.
- 5) We verify our proposed methodology and algorithms via both simulation as well as real-data measurements. We show that our methods can perform better than the existing technique.

**Organisation.** Section II presents the system model, Section III gives details on the FS-SAR methodology by using the composite antenna pattern, Section IV describes the proposed algorithms, i.e., modified back-projection and compressed sensing based back-projection, along with their computational complexities, Section V demonstrates the effectiveness of

the proposed methods via simulation as well as real-data experiments and conclusions are given in Section VI.

**Notations.** Matrices are in upper case bold while column vectors are in lower case bold,  $[\mathbf{X}]_{i,j}$  is the  $ij$ th entry of the matrix  $\mathbf{X}$ ,  $\mathbf{I}_N$  is the identity matrix of size  $N \times N$ ,  $\mathbf{0}_N$  is a vector of zeros of size  $N \times 1$ ,  $(\cdot)^T$  denotes Transpose,  $(\cdot)^H$  is Hermitian,  $(\cdot)^{-1}$  denotes inverse,  $\lfloor \cdot \rfloor$  is the floor function,  $\otimes$  stands for the Kronecker product,  $\star$  describes the convolution,  $\hat{\mathbf{x}}$  is the estimate of  $\mathbf{x}$ ,  $\triangleq$  defines an entity,  $\mathcal{F}\{\cdot\}$  describes a Fourier transform operation,  $\uparrow_{\kappa,\kappa'}(\mathbf{X})$  upsamples the matrix  $\mathbf{X}$  by an order  $\kappa$  along its rows and by an order  $\kappa'$  along its columns,  $\mathcal{O}(\cdot)$  is the big O notation for complexity and the  $\ell_p$ -norm of a vector  $\mathbf{x}$  is denoted as  $\|\mathbf{x}\|_p = (\sum_{i=0}^{N-1} |\mathbf{x}|_i^p)^{1/p}$ .

## II. SYSTEM MODEL

Traditional SAR has two basic modes of operation: *i*) stripmap mode SAR (Strip-SAR), where the radar illuminates a target scene at a fixed look angle (LA) while moving on along its aperture, and *ii*) spotlight mode SAR (Spot-SAR), where the radar illuminates a fixed target scene from multiple LAs. Our proposed FS-SAR mode of operation for Auto-SAR has somethings in common with *i*) and *ii*). At each scan step, the radar scans the target scene at different LAs and then moves on to the next scan step over the aperture. However, in our case, neither the target area remains fixed as in Spot-SAR, nor the LA remains fixed as in Strip-SAR. The contrast between standard SAR modes and FS-SAR mode of Auto-SAR generates new opportunities as well as new challenges. Our aim here is to capitalise on the opportunities and tackle the challenges for an improved radar imaging.

The FS-SAR can schematically be represented as in Figure 1, for 2-D processing. It has multiple scan steps,  $l$ , along the synthetic aperture, i.e.  $l \in [-(L-1)/2, (L-1)/2]$ . For each scan step, the radar scans at multiple LAs,  $\theta$ , with angular range,  $\theta \in [-\theta_{\max}, +\theta_{\max}]$ . The target range,  $r$  is the Euclidean distance between the target and the radar with  $r \in (0, R_{\max}]$ . The target scene is visualised in a Cartesian coordinate system (CCS), i.e., target location is represented as  $(x_i, y_j)$  with  $x_i$  and  $y_j$  being coefficients of  $x$ -axis and  $y$ -axis, respectively. The target can also be represented in a polar coordinate system (PCS), i.e.,  $r_{ij} \angle \theta_{ij}$ , where  $r_{ij} \triangleq \sqrt{x_i^2 + y_j^2}$  and  $\theta_{ij} \triangleq \arctan(y_j/x_i)$  (w.r.t. the current position of radar). Note, Figure 1 shows the radar moving along  $x$ -axis only. However, it is not a limitation of the proposed method and the radar can undertake any kind of motion, in principle.

In our system model, we assume that the radar works on a stop-and-go principle, i.e., the radar is static during the transmission of an FMCW pulse. In general FMCW pulses are long. Therefore, stop-and-go assumption may not remain valid, as there is a possible motion of the radar platform during the transmit pulse, giving rise to the instantaneous Doppler. A number of methods are available to compensate for such a radar motion, both in the frequency domain, e.g., [25], [26] and in the time domain, e.g., [27]. In our case, our proposed algorithms work in the time domain. Therefore, we can easily use the approach of [27] to compensate for the radar motion during the transmit pulse. This essentially comprises of shifting the

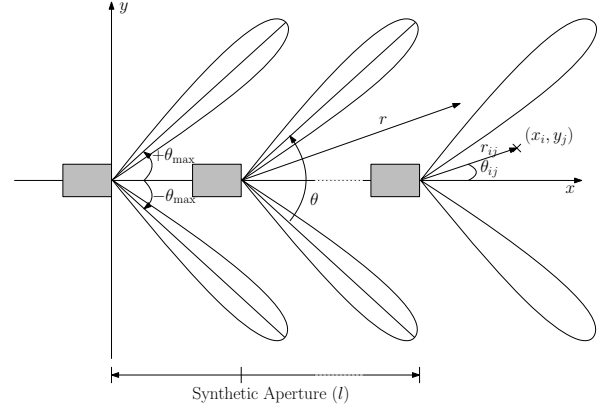


Fig. 1. FS-SAR schematic (2-D).

pulse contributions by a term which is a function of radar velocity and the squint angle between radar and the target. However, to keep the model simple, in this paper we continue with the stop-and-go principle. Nonetheless, extensions for instantaneous Doppler compensation are straightforward and they do not affect our proposed approaches.

Let the generic FMCW transmit pulse be of the form

$$s^{\text{Tx}}(t) = \exp(j2\pi f_0 t + j\pi\beta t^2) \quad (1)$$

where  $f_0$  is the carrier frequency,  $\beta \triangleq B/T$  is the chirp rate defined as the ratio between bandwidth  $B$  of the transmitted signal and pulse repetition interval (PRI)  $T$ , and  $t$  is the fast time variable valid within the PRI, i.e.,  $0 \leq t < T$ . We assume that one such pulse is transmitted at every LA<sup>1</sup>, over the complete aperture. The received signal is the sum of reflections from different scatterers within the radar beamwidth. At  $l$ th scan step and  $\theta$ th LA, the received signal can be written as

$$s_{l,\theta}^{\text{Rx}}(t) = \sum_{u=1}^U \alpha_u \exp(j2\pi f_0 [t - \tau_{l,\theta}(u)] + j\pi\beta [t - \tau_{l,\theta}(u)]^2) \quad (2)$$

where  $\alpha_u$  is the reflectivity coefficient (which includes the effects of range related variations in the back-scattered energy) and  $\tau_{l,\theta}(u)$  is the two-way time delay of the  $u$ th scatterer. Note that the total number of scatterers  $U$  can vary for different scan steps and LAs but we assume them to be the same here for ease of notations. The received signal is mixed with the transmit signal, a process known as deramping, and low-pass filtered, generating an intermediate frequency, also known as beat frequency, corresponding to individual targets. The resulting signal can be written as

$$\begin{aligned} \tilde{s}_{l,\theta}(t) = & \sum_{u=1}^U \alpha_u \exp(j2\pi f_0 \tau_{l,\theta}(u)) \exp(j2\pi\beta \tau_{l,\theta}(u)t) \\ & \times \exp(-j\pi\beta \tau_{l,\theta}^2(u)) \end{aligned} \quad (3)$$

where the frequency of the sinusoid  $\exp(j2\pi\beta \tau_{l,\theta}(u)t)$  carries information regarding target range, which can be easily observed by doing a Fourier analysis of (3), the exponent

<sup>1</sup>Note, one pulse per LA is assumed for the sake of simplicity. However, multiple pulses per LA can also be considered, in principle.



$j2\pi f_0\tau_{l,\theta}(u)$  is important for SAR processing because it traces a target over the aperture, and the exponent  $j\pi\beta\tau_{l,\theta}(u)^2$  is the unwanted phase term, also known as residual video phase (RVP), which can be removed via a deskewing process. Note, the deskewing process essentially applies a frequency dependent filter in order to remove the RVP which is proportional to the delay (i.e., range) [28]. Applying deskewing on (3), we can write,

$$s_{l,\theta}(t) = \mathcal{F}^{-1}\{\mathcal{F}\{s_{l,\theta}(t)\} \exp(j\pi f^2/\beta)\} \\ \approx \sum_{u=1}^U \alpha_u \exp(j2\pi f_0\tau_{l,\theta}(u)) \exp(j2\pi\beta\tau_{l,\theta}(u)t) \quad (4)$$

where  $f$  is the frequency parameter corresponding to  $t$ . The range profile can be generated by taking the Fourier transform of  $s_{l,\theta}(t)$  and then using a linear transformation from the frequency domain axis to the range domain axis [24], i.e.,

$$x_{l,\theta}(r) = \mathcal{F}\{s_{l,\theta}(t)\}|_{r=\frac{f}{2\beta}} \quad (5)$$

where  $r$  being the range variable with linear transformation,  $r = f/2\beta$ . Sampling the range domain at the Nyquist rate means that the range resolution,  $\Delta_r$ , can be defined as,  $\Delta_r \triangleq c/2B$ , and the range bin can be referenced as,  $r_{n_r}$ , for  $n_r = 0, 1, \dots, N_r - 1$ , where,  $N_r \triangleq R_{\max}/\Delta_r$ . Now, let us focus on scene variations along the azimuth, for a specific range bin. From (5), we can represent the target scene reflectivities along azimuth for the  $r_{n_r}$ th range bin by  $x_{l,r_{n_r}}(\theta)$ , i.e.,

$$x_{l,r_{n_r}}(\theta) = \{x_{l,\theta}(r_{n_r})\}_{\theta=-\theta_{\max}}^{+\theta_{\max}}. \quad (6)$$

Note, we drop the subscript  $n_r$  from  $x_{l,r_{n_r}}(\theta)$  in the following. The received signal along the azimuth can be considered as a convolution between the antenna beam and the target scene reflectivities at a given range bin [11]. If  $h(\theta)$  represents the antenna beam of angular length  $2\phi$  (i.e., the antenna beam pattern is uniformly sampled over  $-\phi$  to  $+\phi$ ), then the signal measured along the azimuth, for range  $r$  and scan step  $l$ , can be written as

$$y_{l,r}(\theta) = h(\theta) \star x_{l,r}(\theta) + n_{l,r}(\theta) \quad (7)$$

where  $y_{l,r}(\theta)$  is the measured signal and  $n_{l,r}(\theta)$  is additive white Gaussian noise (AWGN) with element wise variance,  $\sigma^2$ . The angular resolution of a radar is essentially a function of its 3 dB beamwidth, i.e.,  $\theta_{3\text{dB}}$ . Let the azimuth domain is sampled at an angular interval,  $\delta_\theta = \theta_{3\text{dB}}/\zeta$ , where  $\zeta$  is a positive integer and its value depends on the required AR. For very high AR,  $\zeta \gg 1$ . Then, we can represent  $h(\theta)$  as an  $N_h \times 1$  vector,  $\mathbf{h} \triangleq [h(-\phi), h(-\phi + \delta_\theta), \dots, h(+\phi)]^H$ , where,  $N_h = \lfloor 2\phi/\delta_\theta \rfloor + 1$ . Due to physical limitations, the radar is not able to take measurements at as fine an angular sampling interval as  $\delta_\theta$ . Therefore, let the angular interval for measurements is represented as,  $\Delta_\theta = \xi\delta_\theta$ , where  $\xi \geq 1$ . For a very coarse angular measurement interval,  $\xi \gg 1$ . Then, we can represent  $y_{l,r}(\theta)$  as an  $N_\theta \times 1$  vector,  $\mathbf{y}_{l,r} \triangleq [y_{l,r}(-\theta_{\max}), y_{l,r}(-\theta_{\max} + \Delta_\theta), \dots, y_{l,r}(+\theta_{\max})]^H$ , where  $N_\theta = \lfloor 2\theta_{\max}/\Delta_\theta \rfloor + 1$ . Similar to  $h(\theta)$ ,  $x_{l,r}(\theta)$  can be represented as an  $N_x \times 1$  vector,  $\mathbf{x}_{l,r} \triangleq [x_{l,r}(-\tilde{\theta}_{\max}), x_{l,r}(-\tilde{\theta}_{\max} + \delta_\theta), \dots, x_{l,r}(+\tilde{\theta}_{\max})]^H$ , where  $\tilde{\theta}_{\max} \triangleq \theta_{\max} + (N_h - 1)\delta_\theta/2$

and  $N_x = \xi N_\theta + N_h - 1$ . Note, by introducing  $\tilde{\theta}_{\max}$  in  $\mathbf{x}_{l,r}$ , we make sure to account for all the contributing targets within the radar beamwidth, for each measurement. Finally,  $n_{l,r}(\theta)$  can be represented as an  $N_\theta \times 1$  vector,  $\mathbf{n}_{l,r} \triangleq [n_{l,r}(-\theta_{\max}), n_{l,r}(-\theta_{\max} + \Delta_\theta), \dots, n_{l,r}(+\theta_{\max})]^H$ . Thus, we can write (7) in the following discrete form.

$$\mathbf{y}_{l,r} = \mathbf{G}\mathbf{H}\mathbf{x}_{l,r} + \mathbf{n}_{l,r} \quad (8)$$

where  $\mathbf{H}$  is the  $(\xi N_\theta - 1) \times N_x$  Toeplitz matrix, defined as

$$\mathbf{H} \triangleq \begin{pmatrix} \mathbf{h}^H & & \mathbf{0}_{(N_x - N_h)}^T \\ 0 & \mathbf{h}^H & \mathbf{0}_{(N_x - N_h - 1)}^T \\ \vdots & \vdots & \vdots \\ \mathbf{0}_{(N_x - N_h)}^T & & \mathbf{h}^H \end{pmatrix} \quad (9)$$

depicts the convolution between antenna beam pattern and the target scene, and  $\mathbf{G}$  is an  $N_\theta \times (\xi N_\theta - 1)$  selection matrix, i.e.,  $[\mathbf{G}]_{n_\theta,:} = [\mathbf{I}_{(\xi N_\theta - 1)}]_{(\xi n_\theta - \xi + 1),:}$ , for  $n_\theta = 0, 1, \dots, N_\theta - 1$ . Here, we assume  $\mathbf{H}$  to be the same for each scan step as well as for each range bin. This assumption has been considered for the sake of simplicity. However, variations in  $\mathbf{H}$  with different scanning steps can easily be accommodated in the model. Now, for all range bins, we can modify (8) as

$$\mathbf{Y}_l = \mathbf{G}\mathbf{H}\mathbf{X}_l + \mathbf{N}_l \quad (10)$$

where  $\mathbf{Y}_l \triangleq [\mathbf{y}_{l,0}, \mathbf{y}_{l,\Delta_r}, \dots, \mathbf{y}_{l,(N_r\Delta_r - N_r)}]$ ,  $\mathbf{X}_l \triangleq [\mathbf{x}_{l,0}, \mathbf{x}_{l,\Delta_r}, \dots, \mathbf{x}_{l,(N_r\Delta_r - N_r)}]$  and  $\mathbf{N}_l \triangleq [\mathbf{n}_{l,0}, \mathbf{n}_{l,\Delta_r}, \dots, \mathbf{n}_{l,(N_r\Delta_r - N_r)}]$  are  $N_\theta \times N_r$ ,  $N_x \times N_r$  and  $N_\theta \times N_r$  matrices, respectively.

### III. FS-SAR METHODOLOGY

Our main goal is to use SAR concepts to enhance the AR of an Auto-radar. However, Auto-radar functions as an FL-SAR, most of the times. Therefore, standard SAR can make only limited contributions to the AR enhancement. The FS-SAR methodology increases SAR capabilities by scanning the target scene at multiple LAs over the complete aperture. In this section, we show how FS-SAR method can contribute to the AR enhancement of an Auto-radar, by comparing its composite antenna pattern with that of the standard SAR.

#### A. FL-SAR Antenna Pattern

Conceptually, a synthetic aperture is similar to a phased antenna array, in that each point on the aperture can be considered as an antenna element. However, the difference is that all the elements are not activated at the same time and the output of the synthetic array can be computed by adding the individual contributions of each element. The synthetic aperture comprises of the complete stretch of the synthetic array. This is the case for an SL-SAR, i.e., the LA of the radar is normal to the velocity of radar platform. For the FL-SAR, the LA of the radar is not normal to the velocity of the radar platform. Therefore, effective aperture is reduced and this reduction is proportional to the LA. Figure 2 shows the schematic of a SAR, where  $L$  is the total length of the synthetic aperture with  $N_l$  antenna elements of spacing  $\Delta_l$ , i.e.,  $L = N_l\Delta_l$ . At an LA  $\theta_n$ , the effective aperture is given

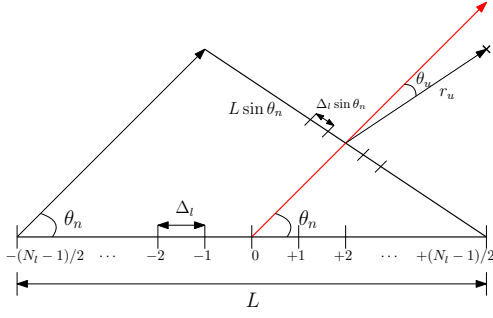


Fig. 2. (FL-)SAR: Synthetic antenna array for LA,  $\theta_n$ .

as  $L \sin \theta_n$  and the element spacing amounts to  $\Delta_l \sin \theta_n$ . To find the antenna pattern of the synthetic array for the  $\theta_n$ th LA, let a continuous signal  $\exp(j2\pi f t)$  is transmitted from  $n_l$ th aperture element, for,  $n_l = -(N_l - 1)/2, \dots, (N_l - 1)/2$ . Given a single target scatterer at a distance  $r_u$  and angle  $\theta_u$  from the  $n_l$ th aperture element, the composite received signal of the synthetic antenna array can be written as

$$\begin{aligned} s_{\theta_n}(t) &= \sum_{n_l} \exp\{j2\pi f(t - 2r_u/c + 2n_l \Delta_l \sin \theta_n \sin \theta_u/c)\} \\ &= C_u \sum_{n_l} \exp\{j2\pi n_l \Delta_l \sin \theta_n \sin \theta_u/\lambda\} \\ &= C_u \frac{\sin(2\pi N_l \Delta_l \sin \theta_n \sin \theta_u/\lambda)}{N_l \sin(2\pi \Delta_l \sin \theta_n \sin \theta_u/\lambda)} \\ &\approx C_u \text{sinc}(2\pi N_l \Delta_l \sin \theta_n \sin \theta_u/\lambda) \end{aligned} \quad (11)$$

where  $C_u \triangleq \exp\{j2\pi f(t - 2r_u/c)\}$ , and we use the approximation,  $\sin(\varphi) \approx \varphi$ , for small  $\varphi^2$ . We can see that (11) generates a symmetric antenna pattern of an FL-SAR. The angular resolution can then be determined by finding the angle at which the sinc function produces a first null. This happens when

$$\sin \theta_u = \frac{\lambda}{2L \sin \theta_n} \quad (12)$$

and the AR can be calculated as

$$\Delta_{\text{AR}}^{\text{FL-SAR}} = \frac{r_u \lambda}{2L \sin \theta_n}. \quad (13)$$

From (13), we can see that the effect of synthetic aperture is maximum when radar functions as SL-SAR. However, in case of FL-SAR, effective aperture decreases proportional to the LA, i.e.,  $\theta_n$ .

### B. FS-SAR Antenna Pattern

In FS-SAR approach, we scan the target scene at multiple LAs for each aperture element. Figure 3 shows the schematic for synthetic array with multiple LAs, parameterised by  $\theta$ . Following (11), we can write the composite signal received at the synthetic array for multiple LAs  $\theta_n$ , for

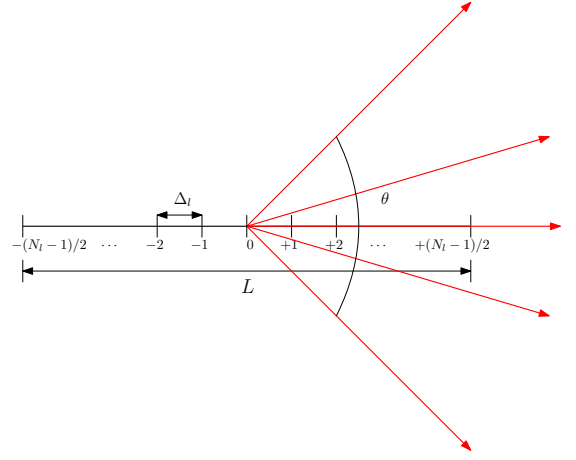


Fig. 3. FS-SAR: Synthetic antenna array, with multiple LAs.

$n = -(N_\theta - 1)/2, \dots, (N_\theta - 1)/2$ , as

$$\begin{aligned} s(t) &= \sum_n s_{\theta_n}(t) \\ &\approx C_u \sum_n \text{sinc}(2\pi N_l \Delta_l \sin \theta_n \sin \theta_u/\lambda) \end{aligned} \quad (14)$$

which also provides the symmetric composite antenna pattern for FS-SAR method. Finding a closed form solution of (14) is difficult. However, in order to find the Rayleigh beamwidth of the composite antenna pattern, we make an approximation. We can see from (11) that for each  $\theta_n$ , the sinc function produces a null when its argument equals  $\pi$ . Following this observation, we can assume that the sum of  $N_\theta$  sinc functions would produce a null when the sum of their arguments equals  $N_\theta \pi$ , approximately, i.e.,

$$\sum_n 2\pi N_l \Delta_l \sin \theta_n \sin \theta_u/\lambda = N_\theta \pi. \quad (15)$$

From (15), we can see that the first null occurs when

$$\sin \theta_u = \frac{N_\theta \lambda}{2L \sum_n \sin \theta_n} \quad (16)$$

and the AR then takes the form

$$\Delta_{\text{AR}}^{\text{FS-SAR}} = \frac{r_u N_\theta \lambda}{2L \sum_n \sin \theta_n}. \quad (17)$$

By comparing (12) and (16), we can understand the basic difference between the standard SAR and the FS-SAR approach. For an FL-SAR with an LA  $\theta_n$ , the effective aperture is given by  $L \sin \theta_n$ , i.e., the aperture is decreased by an amount proportional to the LA. Whereas, for FS-SAR approach, the effective aperture is given by  $L \sum_n \sin \theta_n / N_\theta$ , the aperture is decreased by an amount proportional to the mean of the LAs. Thus, if the target is situated at the boresight of a very low LA, then, coherently adding its reflectivities with returns at slightly higher LAs, can basically increase the effective aperture. Figure 4 shows the simulation results of FL-SAR antenna pattern at different LAs and the composite antenna pattern of FS-SAR approach. For FL-SAR, the beamwidth of antenna pattern increases with decreasing LA. However, the beamwidth of the antenna pattern with FS-SAR approach can

<sup>2</sup>Note, this approximation is used for the sake of compact representation only. However, it is not imperative for the validity of the analysis.

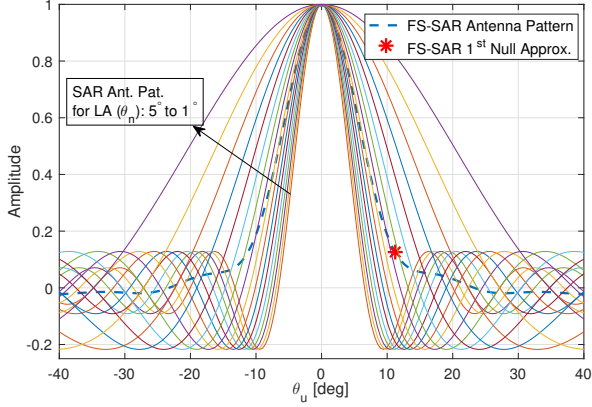


Fig. 4. Composite Antenna Pattern (Normalised).

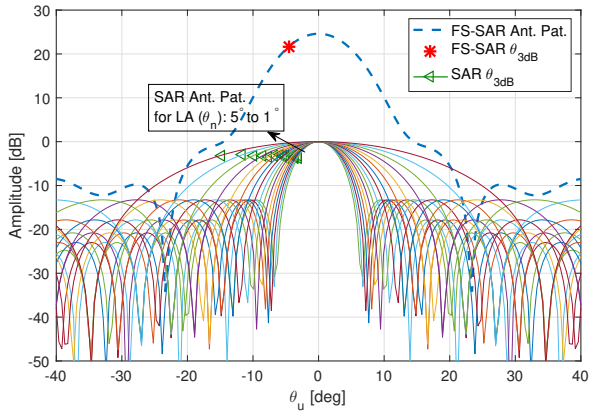


Fig. 5. Composite Antenna Pattern.

be approximated with the mean of the beamwidths of the range of LAs. Figure 4 also shows the approximate value of the 1<sup>st</sup> null for FS-SAR antenna pattern. Note that in Figure 4, we have plotted a normalized version of the FS-SAR antenna pattern. The effect of FS-SAR approach is not only in terms of improvement in the effective aperture, but also in terms of an increase in the composite antenna gain. Figure 5 shows the antenna patterns with actual values of the antenna gains. We can see that the FS-SAR approach exhibits higher antenna gains which are proportional to the range of LAs. We also mark the  $\theta_{3dB}$  points for all the cases. Here too, we can see that the 3 dB beamwidth of the FS-SAR approach can be approximated as the average of 3 dB beamwidths of FL-SAR at different LAs.

#### IV. FS-SAR ALGORITHMS

In this section, we provide two algorithms to implement FS-SAR methodology. Our approach is based on BP. Despite high computational requirements of BP, its flexibility for different SAR mode of operations makes it a feasible candidate for generating image of an Auto-radar. In this section, we also provide insights into reducing computational complexity of our proposed algorithms.

##### A. Modified Back-Projection

We first introduce a modified version of BP. The basic principle of BP is to project all the measurements from each scanning step, on the aperture, back to the target location. Thus, measurements corresponding to the target location from all the scanning steps are coherently combined to generate a composite response of the synthetic aperture<sup>3</sup>. To this end, the measurements are upsampled via interpolation in order to correspond to a finer location grid in range, and subsequently integrated over the aperture to generate a SAR image. In our case, along with range domain, we gain extra information from the angular domain. Therefore, the interpolation can be done both in the range as well as in the azimuth. This phenomenon leads to the modification of the standard BP.

Let us represent  $\mathbf{Y}_l$  from (10) in its upsampled form, by means of interpolation (in both range and azimuth) as,  $\uparrow_{\kappa, \kappa'}(\mathbf{Y}_l)$ , where,  $\uparrow_{\kappa, \kappa'}(\cdot)$  denotes an upsampling function which interpolates a matrix by an order  $\kappa$  along its rows and by an order  $\kappa'$  along its columns<sup>4</sup>. Note, we assume  $\kappa = \kappa'$ , in our case<sup>5</sup>. Given the target scene in CCS, the reconstructed image via modified BP (MBP) can be written as

$$\gamma_{ij}^{\text{MBP}} = \sum_{\theta} \sum_l [\uparrow_{\kappa, \kappa'}(\mathbf{Y}_l)]_{\theta, I_{r_{ij}}} \quad (18)$$

where  $I_{r_{ij}}$  is the column index in  $\uparrow_{\kappa, \kappa'}(\mathbf{Y}_l)$  corresponding to range  $r_{ij} = \sqrt{(x_i - l)^2 + y_j^2}$ . Now, the following remarks regarding image reconstruction via MBP in (18) are in order.

- 1) The measurements are upsampled via interpolation over both the azimuth and the range domains.
- 2) Unlike traditional BP (where either the LA is fixed, i.e., for the case of Strip-SAR, or target range is fixed, i.e., for the case of Spot-SAR), the target information lies both in the range and the LAs, which is exploited by integrating over the aperture as well as over the angle.
- 3) Accumulation of back scattered energy over the angle and the aperture domains results in enhanced AR and better radar image reconstruction.

##### B. Compressed Sensing Based Back-Projection

The FS-SAR method generates target information over both the aperture and the angular domains. Thus, the target response can be greatly increased. The MBP algorithm is essentially an MF operation in both the angle and the aperture domains. It has the ability of capturing all of the target back-scattered energy. However, it is not efficient in creating stark contrast of reflectivity between neighbouring scatterers. To this end we use CS, so that the radar image should consist of very bright scatterers only, and the insignificant scatterers are suppressed. Our approach here is to use CS for each step on the aperture and then use standard BP to fulfil SAR processing.

Given the  $l$ th aperture step, we can apply CS over the azimuth

<sup>3</sup>Note, this is essentially a matched filtering operation in the aperture domain.

<sup>4</sup>Note, interpolation by an order  $\kappa$ , basically inserts  $2^\kappa - 1$  sample points between the original samples, where the values of the newly interpolated sample points depend upon the type of interpolation used.

<sup>5</sup>Traditionally, an upsampling factor of  $\kappa = 2$  can provide substantial gains.

for each range bin, or we can apply CS jointly for all the range bins within the maximum range at  $l$ th aperture step. In this paper, we choose the latter. In this manner we can exploit target features for a wide range of scene targets. Let us rewrite (10) in the following vectorised form.

$$\mathbf{y}_l = \underbrace{[\mathbf{I}_{N_r} \otimes (\mathbf{G}\mathbf{H})]}_{\triangleq \Phi} \mathbf{x}_l + \mathbf{n}_l \quad (19)$$

where  $\mathbf{y}_l \triangleq \text{vec}(\mathbf{Y}_l)$ ,  $\mathbf{x}_l \triangleq \text{vec}(\mathbf{X}_l)$  and  $\mathbf{n}_l \triangleq \text{vec}(\mathbf{N}_l)$  are  $N_\theta N_r \times 1$ ,  $N_x N_r \times 1$  and  $N_\theta N_r \times 1$  vectors, respectively, and  $\Phi \triangleq [\mathbf{I}_{N_r} \otimes (\mathbf{G}\mathbf{H})]$  is an  $N_\theta N_r \times N_x N_r$  joint measurement matrix. Since  $N_\theta \ll N_x$ , (19) is an under-determined system of linear equations. Therefore, CS techniques can be helpful in finding an estimate of  $\mathbf{x}_l$ . This is generally done by solving the following optimisation problem (OP).

$$\hat{\mathbf{x}}_l = \arg \min_{\mathbf{x}_l} \|\mathbf{y}_l - \Phi \mathbf{x}_l\|_2^2 + \lambda \|\mathbf{x}_l\|_1 \quad (20)$$

where  $\lambda > 0$ . For (20) to provide a stable and unique solution, the CS framework puts certain conditions on the measurement matrix (i.e.,  $\Phi$  in our case), in order to guarantee the uniqueness and optimality of the sparse solution. One parameter of these conditions (which is easily verifiable as well) is known as mutual coherence (MC) [29]. MC is defined as the maximum absolute value of the inner product of different columns of the measurement matrix. It basically indicates the interdependence of the columns. In general, a lower value of MC can provide better results. Another parameter (which can be related to MC) is known as restricted isometry property (RIP) [30]. A measurement matrix (with unit normalised columns) is said to satisfy RIP of order  $K$ , given  $\delta_K \in (0, 1)$ , if

$$(1 - \delta_K) \leq \frac{\|\Phi \mathbf{x}_l\|_2^2}{\|\mathbf{x}_l\|_2^2} \leq (1 + \delta_K) \quad (21)$$

where  $K = \|\mathbf{x}_l\|_0^0$ . In general terms, it means that the matrix  $\Phi$  preserves Euclidean length of  $\mathbf{x}_l$  and that every submatrix of  $\Phi$  with less than  $K$  columns acts like an orthonormal matrix. The effect of these performance parameters generally boils down to a relationship between the number of measurements and the number of unknown nonzero elements to be estimated, i.e.,  $K$ , for different measurement matrices, e.g., Gaussian, Bernoulli and partial Fourier matrices [31]. A common characteristic of these measurement matrices is some form of randomness which makes sure that the elements in these matrices are spread out, i.e., their values are not concentrated on any specific location. In our case, the measurement matrix corresponds to the measurements taken at uniform angular interval  $\Delta_\theta$ . In order to conform to the conditions of MC and RIP, we can either, *i*) take measurements at completely random angular intervals, i.e.,  $\Delta_\theta$  is a random variable, or *ii*) introduce jitter to the uniform sampling interval [32], i.e., the angular sampling interval becomes  $\Delta_\theta + \vartheta_{n_\theta}$ , where  $\vartheta_{n_\theta}$  is an independent random variable for,  $n_\theta = 0, 1, \dots, N_\theta - 1$ . The choice between *i*) and *ii*) depends on the possibility of their implementation in hardware. However, generally, angular samples are available for uniform intervals only. Some works, e.g., [23], provide heuristic assessments for using uniform angular samples to obtain reasonable performance results. In this

paper, we continue with the measurements obtained at uniform angular intervals. However, it is clear that the availability of better measurement matrices would only provide even better results.

The OP in (20) is known as least absolute shrinkage and selection operator (LASSO) [33]. Its basic characteristic is to generate a sparse estimate of  $\mathbf{x}_l$ , where the order of sparsity is determined by the parameter  $\lambda$ . However, LASSO is devoid of exploiting any inherent structure in the elements of  $\mathbf{x}_l$ , other than element wise sparsity. A road scene, generally, consists of objects, e.g., cars, cycles, poles, etc., which have a continuum of a reflective surface. In this backdrop, it is better to use an OP which retrieves the correlations between consecutive elements of  $\mathbf{x}_l$ . To this end, we propose to use fused LASSO (F-LASSO) [34] for Auto-radar imaging. The F-LASSO OP can be written as

$$\hat{\mathbf{x}}_l = \arg \min_{\mathbf{x}_l} \|\mathbf{y}_l - \Phi \mathbf{x}_l\|_2^2 + \lambda \|\mathbf{x}_l\|_1 + \lambda_f \|\mathbf{D} \mathbf{x}_l\|_1 \quad (22)$$

where  $\lambda_f$  is a fusion penalty parameter (nonzero and positive) and  $\mathbf{D}$  is the  $N_x N_r \times N_x N_r$  fusion matrix, defined as

$$\mathbf{D} \triangleq \begin{pmatrix} -1 & +1 & 0 & 0 & \cdots & 0 & 0 \\ 0 & -1 & +1 & 0 & \cdots & 0 & 0 \\ \vdots & \vdots & \vdots & \vdots & \vdots & \vdots & \vdots \\ 0 & 0 & 0 & 0 & \cdots & -1 & +1 \\ 0 & 0 & 0 & 0 & \cdots & 0 & +1 \end{pmatrix} \quad (23)$$

with the result that  $\|\mathbf{D} \mathbf{x}_l\|_1 = \sum_{m=1}^{N_x N_r - 1} \|\mathbf{x}_l\|_m - \|\mathbf{x}_l\|_{m-1}\|_1$ , i.e., it relates to the difference of consecutive elements in  $\mathbf{x}_l$ . Thus, F-LASSO penalises both the elements of  $\mathbf{x}_l$  as well as their difference by an  $\ell_1$ -norm. As a consequence, the reconstructed signal is parsimonious but also exhibits smooth transitions over its elements. This phenomenon leads to enhanced AR as well as an improved radar image.

The cost function in OP (22) is convex, in principle. However, for large-scale problems, iterative solvers are preferred. Since the cost function in (22) is neither continuously differentiable, nor separable in the elements of  $\mathbf{x}_l$ , we suggest to use an alternating direction method of multipliers (ADMM) [35], [36] based solver to estimate  $\mathbf{x}_l$  (i.e.,  $\hat{\mathbf{x}}_l$ ) in (22). Now, let the estimate  $\hat{\mathbf{x}}_l$  is reshaped into an  $N_x \times N_r$  matrix  $\hat{\mathbf{X}}_l^6$ . By using  $\hat{\mathbf{X}}_l$ , the radar image can be reconstructed via CS based BP (CBP) as

$$\gamma_{ij}^{\text{CBP}} = \sum_l [\uparrow_{1,\kappa}(\hat{\mathbf{X}}_l)]_{I_{\theta_{ij}}, I_{r_{ij}}} \quad (24)$$

where  $I_{\theta_{ij}}$  is the row index and  $I_{r_{ij}}$  is the column index in  $\uparrow_{1,\kappa}(\hat{\mathbf{X}}_l)$ , corresponding to angle  $\theta_{ij} = \arctan((x_i - l)/y_j)$  and range  $r_{ij}$ , respectively. Now, the following remarks regarding image reconstruction via CBP in (24) are in order.

- 1) Upsampling via interpolation is done in the range domain, whereas upsampling in the azimuth domain might be unnecessary since CS based reconstruction provides ample upsampling itself.
- 2) Integration is done only over the aperture domain. Since CS based reconstruction is in the angle domain, it

<sup>6</sup>Note, this is just a reverse operation of  $\hat{\mathbf{x}}_l = \text{vec}(\hat{\mathbf{X}}_l)$ .

provides better alternative to MF operation, resulting in sparse reconstruction.

- 3) By combining CS based reconstruction over the angle domain with SAR processing, (24) guarantees enhanced AR and a better Auto-radar image.

### C. Computational Complexity

Our proposed algorithms essentially build upon BP. Therefore, the computational complexity of our algorithms is primarily determined by the implementation of BP. A number of techniques have been proposed in the literature to reduce the computational complexity of BP, e.g., [37]–[39]. In this section we explain how these techniques can be used in connection with our proposed algorithms to reduce the overall computational complexity.

Let the target scene is represented by an  $N \times N$  pixel image/grid in CCS. Then, the computational complexity of BP is equivalent to collecting the total number of operations involved in finding the contribution of each image pixel in every measurement of the target scene. In this respect, the computational complexity of MBP can be written as

$$\mathcal{C}^{\text{MBP}} = \mathcal{O}(N_\theta N_l N^2) \quad (25)$$

where  $\mathcal{O}(\cdot)$  denotes the order of complexity<sup>7</sup>. From (25) we can see that the major source of computation is to back project every measurement over the whole pixel grid. As pointed out in [37], if a subset of measurements (where the subset can be chosen based on the property of nearness among measurements) is back projected on a Polar grid, we can reduce the frequency of mapping the measurements to the Cartesian grid. In our case, the angular measurements at a particular aperture position, share a common point of reference. Therefore, we can back project all of the angular measurements on the Polar grid, in principle, and then map the measurements to the Cartesian grid for a particular aperture position.

Similar ideas can be utilised to reduce computational complexity over the aperture domain as well. The basic principle of all types of fast implementations of BP over the aperture domain is as follows: Partition the aperture into small sub-apertures, each subaperture corresponds to a coarse resolution so requires low computational complexity, combine all the subapertures into a final high resolution image. This aperture partitioning and combining can either be of a single level [37] or of multiple/hierarchical levels [38]. In the light of the above discussion, the computational complexity of our MBP algorithm can be generalized as

$$\mathcal{C}^{\text{MBP}} \approx \mathcal{O}(\log_b(N_l) N^2) \quad (26)$$

where  $\log_b(N_l)$  is the number of hierarchical levels of the aperture in fast implementation of BP and  $b$  is the factorisation basis<sup>8</sup>.

For CBP, the computational complexity over the aperture is the same as that of the MBP. However, in the angular domain,

<sup>7</sup>Note, here we have ignored the complexity of operations involved in upsampling/interpolation

<sup>8</sup>Note,  $b = 3$  has been found to be the optimal factorisation basis [40].

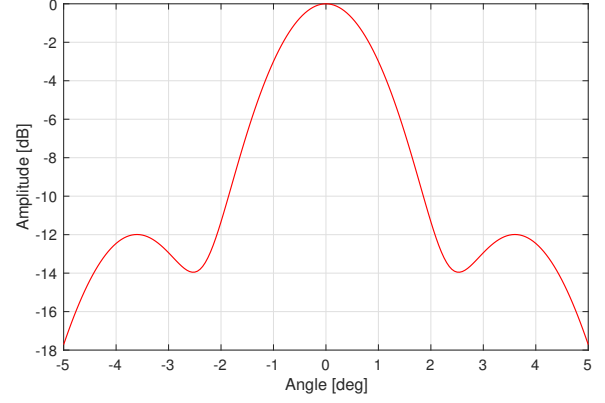


Fig. 6. Antenna Pattern.

the computational complexity depends upon the reconstruction algorithm used to estimate  $\mathbf{x}_l$ . Most of the CS reconstruction algorithms have cubic or quadratic order of complexity. However, iterative approaches can have computational complexity lesser than quadratic. Nonetheless, CS based reconstruction in CBP is carried out in the angle domain. Therefore, the reconstructed image is automatically defined on a Polar grid. Thus, the computational complexity of CBP can generally be approximated to be similar to that of MBP, i.e.,  $\mathcal{C}^{\text{CBP}} \approx \mathcal{C}^{\text{MBP}}$ .

## V. EXPERIMENTAL VERIFICATION

In this section, we provide the experimental verification of our proposed algorithms and methodology via simulation as well as real-data experiments. We consider an FMCW monostatic radar operating at carrier frequency,  $f_0 = 150$  GHz. We consider the radar signal bandwidth as,  $B = 6$  GHz. Therefore, the range resolution can be calculated as,  $\Delta_r = 2.5$  cm.

### A. Simulation

Following the radar specifications of [4], the 3 dB beamwidth of the horn antenna (for the considered radar) can be approximated as,  $\theta_{3\text{dB}} \approx 2^\circ$ . As is clear from Section II, knowledge of the exact beam pattern is essential for AR improvement, so we consider the beam pattern of a horn antenna as described by [41], which can be related to a mixture of Gaussian pdfs, i.e.,

$$h^2(\theta) = \sum_k a_k \exp((\theta - \mu_k)^2 / \sigma_\theta^2) \quad (27)$$

where variance  $\sigma_\theta^2$  is set according to  $\theta_{3\text{dB}}$ , and coefficients  $a_k$  and positions  $\mu_k$  are adjusted deterministically to emulate the beam pattern suggested by [41]. Figure 6 shows such a beam pattern that has been used in our simulations. Notice the presence of sidelobes in the beam pattern. Their role can be crucial in determining the success of any AR enhancement methodology.

We consider the target scene as a grid, i.e., consisting of cells, in the CCS. A target may occupy a number of cells (i.e., an



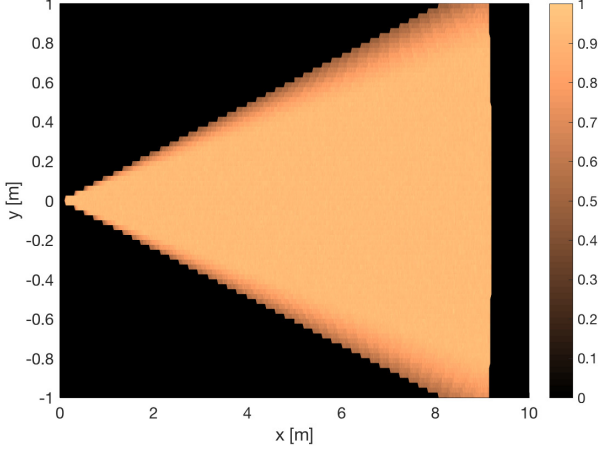


Fig. 7. Auto-radar measurement path.

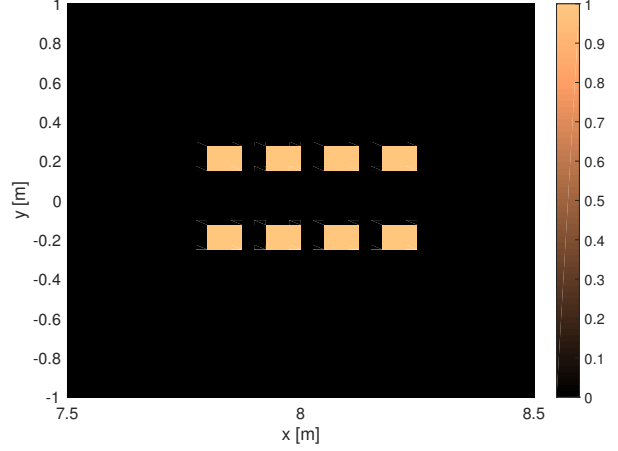


Fig. 8. Target Scene in the CCS.

extended target). We consider the size of these cells equal to the range resolution in both axes. For the simulation, we assume the target scene to be an area of  $2 \times 10 \text{ m}^2$ . The radar moves along the  $x$ -axis at  $y = 0$ . However, this movement pattern is just for the sake of presentation and does not limit the proposed methods. Figure 7 shows the radar path. Over the aperture, we consider  $N_l = 5$  aperture steps with the distance of  $\Delta_l = 5 \text{ cm}$  between consecutive steps. Due to the FS-SAR methodology, the target area which is visited by radar more than other areas, acquires higher back-scattered energy. This can be seen in Figure 7 by areas lit up with higher intensity. We consider  $\theta_{\max} = 7^\circ$ . Therefore, the radar scans from  $-7^\circ$  to  $+7^\circ$ , with angular steps,  $\Delta_\theta = 0.2^\circ$ . Maximum range for each scan is limited to,  $R_{\max} = 9 \text{ m}$ .

We set up a target scene which exhibits the nature of a typical road scene, i.e., consisting of extended targets. We consider eight target objects. Each target spans  $5 \times 3$  group of cells. The distance between the objects along  $x$ -axis (which can be related to the range in our case), consists of two cells, i.e.,  $5 \text{ cm}$ . The distance between the objects along  $y$ -axis (which can be related to the azimuth in our case), consists of ten cells, i.e.,  $25 \text{ cm}$ . Figure 8 shows the target scene. We generate measurements of the target scene according to (7). We assume AWGN for an SNR of  $10 \text{ dB}$ . The SNR is defined in terms of (19) as

$$\text{SNR} \triangleq \frac{\|\Phi \mathbf{x}_l\|_2^2}{N_\theta N_r \sigma^2}. \quad (28)$$

We generate measurements for every LA at every aperture step. However, we represent them collectively in Figure 9, superimposed on each other. We can see that the objects are distinguishable in the range domain, primarily because of the fine range resolution of the radar. However, the azimuth domain cannot resolve the target objects.

Figure 10 shows the result of reconstructing the image via MBP. In comparison to unprocessed measurements, the image constructed via MBP is better. The target objects in the azimuth domain are not strikingly apart. However, we can see a border distinguishing the objects. Figure 11 shows the reconstructed image via CBP. We see better results than MBP.

Each object has been reconstructed in its entirety. Target objects are clearly distinguishable both in the range as well as in the azimuth domain. The image is also free from any specular artefacts. Note that for CBP, we chose iterative solvers to estimate  $\mathbf{x}_l$  in (22). The tuning parameters  $\lambda$  and  $\lambda_f$  can be chosen via a cross validation procedure [42]. For the sake of comparison, we also construct the image with OMP. Note, OMP essentially solves an  $\ell_0$ -norm (constrained) OP, instead of an  $\ell_1$ -norm (unconstrained) OP in (20). Figure 12 shows the reconstructed image. We can see that our proposed CBP approach performs much better than OMP. This is because of the inherent properties of the F-LASSO, i.e., to preserve target features as well as create parsimony in the solution.

### B. Real Data

In this section, we apply our proposed algorithms on the real data obtained via the FS-SAR methodology in controlled laboratory conditions, as an illustration. We consider two trolleys, separated by a certain distance, as our targets which is akin to two cars side-by-side. The size of a trolley equals (approx.)  $1 \times 0.5 \times 0.55$  (length  $\times$  width  $\times$  height)  $\text{m}^3$ . We consider two values for separation, i.e.,  $15 \text{ cm}$  and  $5 \text{ cm}$ . Figure 13 shows the targets. It also shows a center line which provides a trajectory of the radar movement, i.e., the radar moves along this line. We can see that the targets are offset from this center line. We consider an offset angle of  $5^\circ$  from the centre of the synthetic aperture. In order to create a synthetic aperture, we use a rail, as shown in Figure 14. The radar moves over this rail and scans the scene at different positions over the aperture. The length of the rail is  $L = 1.8 \text{ m}$  and the distance of the target centre from the start of the center line is  $8.6 \text{ m}$ . We take aperture samples at  $2.5 \text{ cm}$ , with  $N_l = 73$  samples in total. At each step on the aperture, the radar scans the target scene from  $-10^\circ$  to  $+20^\circ$  at angular steps  $\Delta_\theta = 0.25^\circ$ . Figure 15 provides a schematic of this scenario.

We first measured the antenna pattern of the radar since its accurate measurement is essential for the azimuth processing. Figure 16 shows the measured antenna pattern with  $\theta_{3\text{dB}} \approx 1.3^\circ$ . Note, Table I provides the complete specifications of

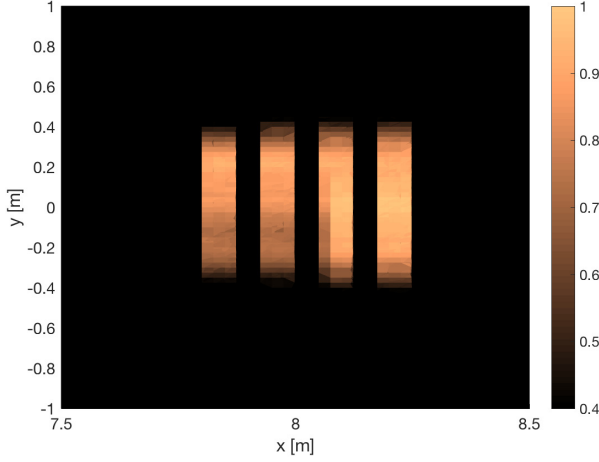


Fig. 9. Measured Scene.

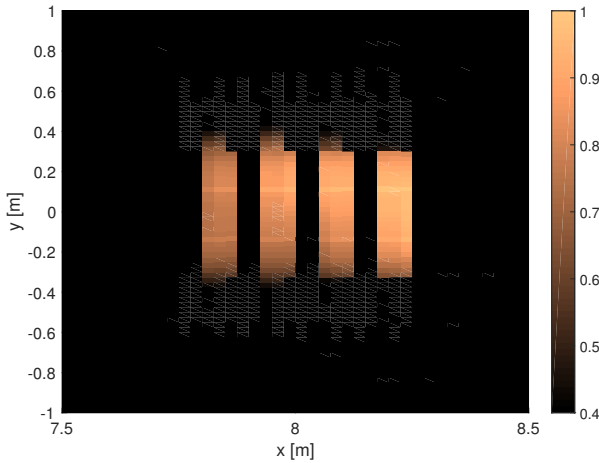


Fig. 10. Reconstructed image via MBP.

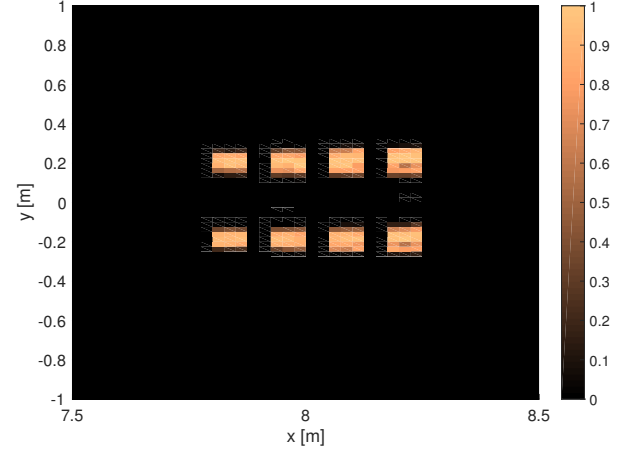


Fig. 11. Reconstructed image via CBP.

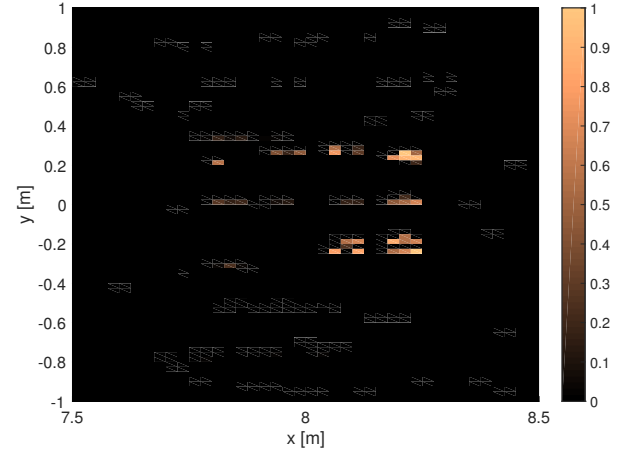


Fig. 12. Reconstructed image via OMP.

the 150 GHz radar. Then, we took the scene measurements. Figures 17 and 18 show the measured scenes when radar is closest to the targets over the aperture, for an inter-target separation of 15 cm and 5 cm, respectively. Note, we do not get any reflections from the middle walls of the trolleys. Therefore, the azimuth refinement concerns the recognition of corners of the trolley. We focus on the front corners of the trolleys facing each other, highlighted by a dotted ellipse. We can see from figures 17 and 18 that front corners are not distinguishable. Also, the radar image has missed substantial details of the trolley. In contrast, the image reconstructed via MBP as shown by figures 19 and 20, provides a better recognition of the corners of the trolleys, i.e., the separating grooves are better pronounced. Also, substantial details of the trolleys have been captured. Note, in our setting, the slant range from the aperture center to the center of targets is approximately 7 m. With  $\theta_{3dB} = 1.3^\circ$ , this amounts to AR of over 15 cm. From 20, we can see that by using MBP, we have been able to enhance AR almost by a factor of 3. Figures 21 and 22 show the results of reconstructing the image via CBP. We can see that the performance of CBP is even better than MBP. Thus, we can say that our proposed methods can provide significant gains

TABLE I  
SPECIFICATIONS OF 150 GHz RADAR

Modulation	FMCW
Frequency Range	145 – 151 GHz
Transmit Bandwidth ( $B$ )	6 GHz
Chirp Duration ( $T$ )	1.2 ms
Sampling Frequency	5 MHz
Angular Step ( $\Delta\theta$ )	$0.25^\circ$
Range Resolution ( $\Delta_r$ )	0.025 m
3 dB Beamwidth ( $\theta_{3dB}$ )	$1.3^\circ$

to enhance AR and improve imaging of an FS-SAR.

Note, Figures 19-22 essentially provide a qualitative analysis of the FS-SAR methodology. However, a quantitative analysis of this methodology can be obtained by plotting (17) for different angular ranges of the scan. Figure 23 provides such an analysis for varying ranges. Since our experimental set up falls in the angular range  $\theta_n \in [0^\circ, 15^\circ]$ , we can see that at a 10 m range, the AR of FS-SAR is (approx.) 4 – 5 cm, which is matched by the performance of our algorithms. Therefore, the performance of FS-SAR methodology is consistent both qualitatively as well quantitatively.

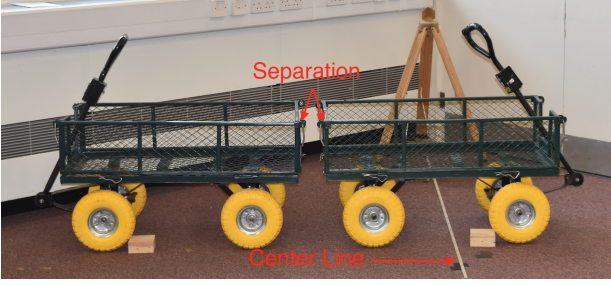


Fig. 13. Target Scene.

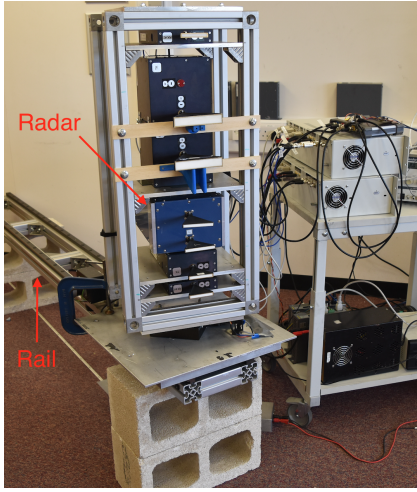


Fig. 14. Radar and the Rail.

## VI. CONCLUSIONS

In this paper, we have presented signal processing techniques to deliver Auto-radar imaging with improved angular resolution. We have used frequency modulated continuous wave signalling for a THz radar. We have proposed an FS-SAR methodology. We have shown that FS-SAR methodology causes an improvement in the effective aperture and an increase in the composite antenna gain. Thus, it results in the enhancement of angular resolution. We have proposed two algorithms, namely, modified back-projection and compressed sensing based back-projection, in order to capitalise on the gains of the FS-SAR technique. Both algorithms provide improved imaging. However, the latter has an edge over the former because it exploits the sparsity of the scene. The computational complexity of our proposed algorithms can also be easily managed. Results of simulation and real-data experiments prove the validity of our proposed methods. Future work consists of applying the proposed methods for imaging the moving targets in the presence of clutter.

## ACKNOWLEDGEMENTS

This work has been approved for submission by TASSC-PATHCAD sponsor, Chris Holmes, Senior Manager Research, Research Department, Jaguar Land Rover, Coventry, UK.

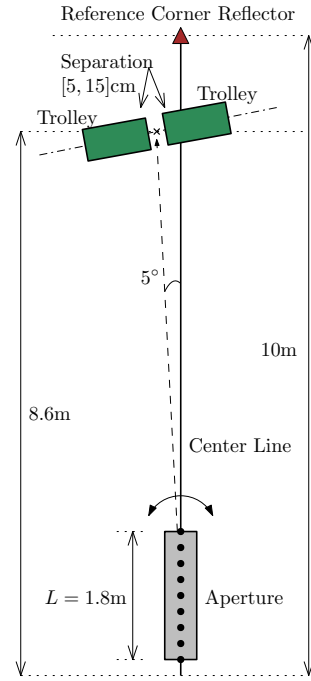


Fig. 15. Real Data Measurement Scenario.

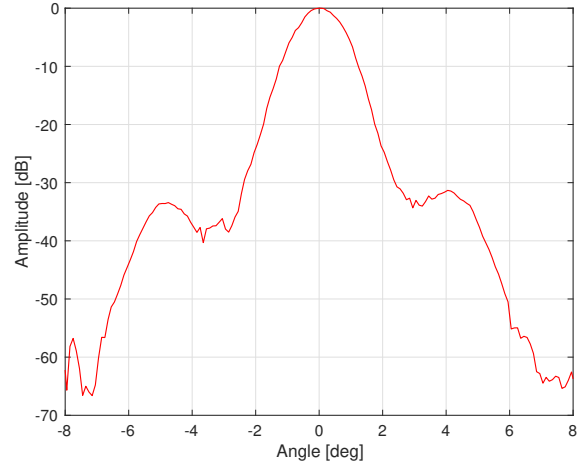


Fig. 16. Measured Antenna Pattern.

## REFERENCES

- [1] K. Bengler, K. Dietmayer, B. Farber, M. Maurer, C. Stiller, and H. Winner, "Three decades of driver assistance systems: Review and future perspectives," *IEEE Intelligent Transportation Systems Magazine*, vol. 6, no. 4, pp. 6–22, winter 2014.
- [2] A. Eskandarian, *Handbook of Intelligent Vehicles*. NY, USA: Springer-Verlag, 2012.
- [3] E. Guizzo, "How Google's self-driving car works," *IEEE Spectrum Online*, vol. 18, 2011.
- [4] D. Jasteh, E. G. Hoare, M. Cherniakov, and M. Gashinova, "Experimental low-terahertz radar image analysis for automotive terrain sensing," *IEEE Geoscience and Remote Sensing Letters*, vol. 13, no. 4, pp. 490–494, April 2016.
- [5] M. Murad, I. Bilik, M. Friesen, J. Nickolaou, J. Salinger, K. Geary, and J. S. Colburn, "Requirements for next generation automotive radars," in *IEEE Radar Conference (RadarCon13)*, April 2013, pp. 1–6.
- [6] S. M. Patole, M. Torlak, D. Wang, and M. Ali, "Automotive radars: A review of signal processing techniques," *IEEE Signal Processing Magazine*, vol. 34, no. 2, pp. 22–35, March 2017.



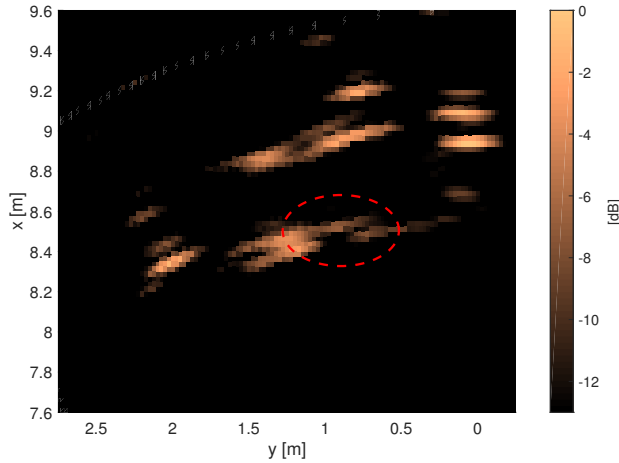


Fig. 17. Measured Scene: Closest to the targets at 15 cm separation.

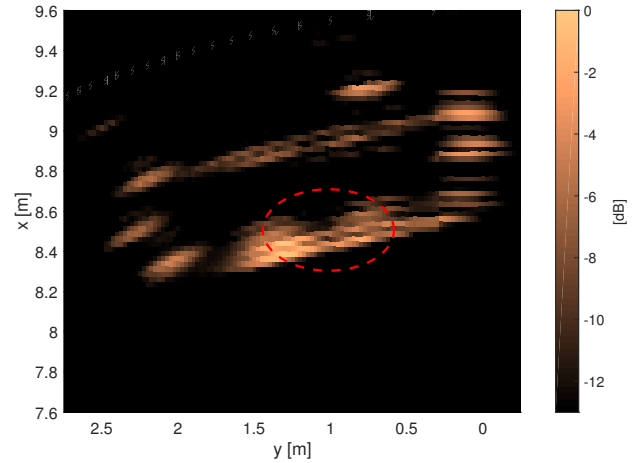


Fig. 19. Reconstructed image via MBP: 15 cm separation.

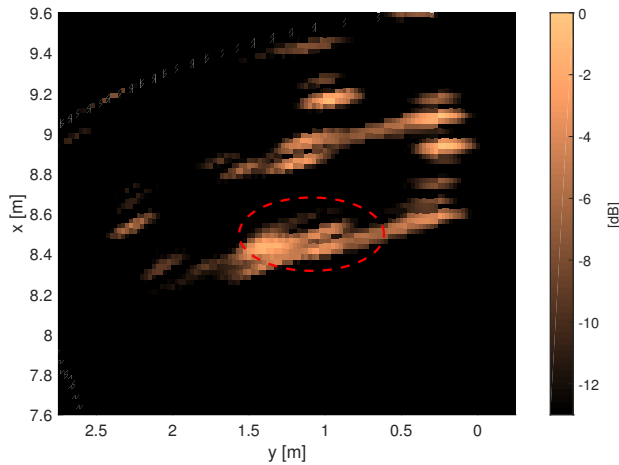


Fig. 18. Measured Scene: Closest to the targets at 5 cm separation.

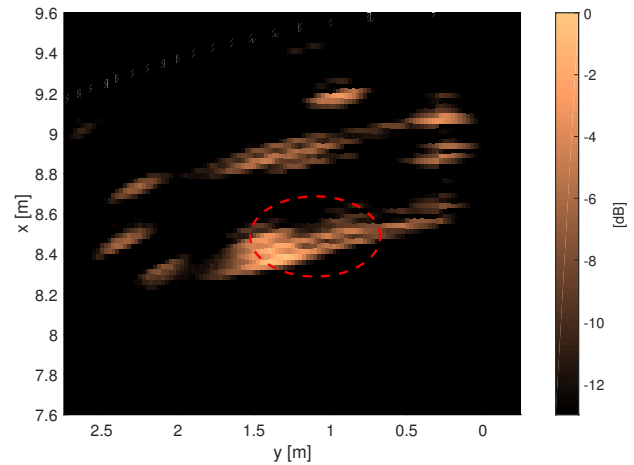


Fig. 20. Reconstructed image via MBP: 5 cm separation.

- [7] G. Krieger, J. Mittermayer, S. Buckreuss, M. Wendler, T. Sutor, F. Witte, and A. Moreira, "Sector imaging radar for enhanced vision," *Aerospace Science and Technology*, vol. 7, no. 2, pp. 147 – 158, 2003.
- [8] A. Farina, F. Gini, and M. Greco, "DOA estimation by exploiting the amplitude modulation induced by antenna scanning," *IEEE Transactions on Aerospace and Electronic Systems*, vol. 38, no. 4, pp. 1276–1286, Oct 2002.
- [9] G. Liu, K. Yang, B. Sykora, and I. Salha, "Range and azimuth resolution enhancement for 94 GHz real-beam radar," in *Proceedings of SPIE on Radar Sensor Technology XII*, vol. 6947, 2008, pp. 1–9.
- [10] S. Uttam and N. A. Goodman, "Superresolution of coherent sources in real-beam data," *IEEE Transactions on Aerospace and Electronic Systems*, vol. 46, no. 3, pp. 1557–1566, July 2010.
- [11] M. A. Richards, *Fundamentals of Radar Signal Processing*. Two Penn Plaza, NY, USA: McGraw-Hill Companies, Inc., 2005.
- [12] M. A. Richards, "Iterative noncoherent angular superresolution [radar]," in *Proceedings of the IEEE National Radar Conference*, Apr 1988, pp. 100–105.
- [13] S. D. Blunt and K. Gerlach, "Adaptive pulse compression via MMSE estimation," *IEEE Transactions on Aerospace and Electronic Systems*, vol. 42, no. 2, pp. 572–584, April 2006.
- [14] M. Ruggiano, E. Stolp, and P. van Genderen, "Improvement of target resolution in azimuth by Immse technique," in *European Radar Conference (EuRAD)*, Sept 2009, pp. 230–233.
- [15] J. Guan, J. Yang, Y. Huang, and W. Li, "Maximum a posteriori based angular superresolution for scanning radar imaging," *IEEE Transactions on Aerospace and Electronic Systems*, vol. 50, no. 3, pp. 2389–2398, July 2014.
- [16] F. Lenti, F. Nunziata, M. Migliaccio, and G. Rodriguez, "Two-dimensional TSVD to enhance the spatial resolution of radiometer data," *IEEE Transactions on Geoscience and Remote Sensing*, vol. 52, no. 5, pp. 2450–2458, May 2014.
- [17] Y. Huang, Y. Zha, Y. Wang, and J. Yang, "Forward looking radar imaging by truncated singular value decomposition and its application for adverse weather aircraft landing," *Sensors*, vol. 15, no. 6, pp. 14 397–14 414, 2015.
- [18] D. L. Donoho, "Compressed sensing," *IEEE Transactions on Information Theory*, vol. 52, no. 4, April 2006.
- [19] E. Candes, J. Romberg, and T. Tao, "Robust uncertainty principles: exact signal reconstruction from highly incomplete frequency information," *IEEE Transactions on Information Theory*, vol. 52, no. 2, pp. 489–509, Feb. 2006.
- [20] L. C. Potter, E. Ertin, J. T. Parker, and M. Cetin, "Sparsity and compressed sensing in radar imaging," *Proceedings of the IEEE*, vol. 98, no. 6, pp. 1006–1020, June 2010.
- [21] M. A. Herman and T. Strohmer, "High-resolution radar via compressed sensing," *IEEE Transactions on Signal Processing*, vol. 57, no. 6, pp. 2275–2284, June 2009.
- [22] S. I. Kelly, G. Rilling, M. Davies, and B. Mulgrew, "Iterative image formation using fast (re/back)-projection for spotlight-mode SAR," in *IEEE RadarCon (RADAR)*, May 2011, pp. 835–840.
- [23] X. Wen, G. Kuang, J. Hu, R. Zhan, and J. Zhang, "Forward-looking imaging of scanning phased array radar based on the compressed sensing," *Progress In Electromagnetics Research*, vol. 143, pp. 575–604, 2013.
- [24] M. Soumekh, *Synthetic Aperture Radar*. River Street, Hoboken, NJ, USA: John Wiley & Sons, Inc., 1999.
- [25] A. Meta, P. Hooeboom, and L. P. Ligthart, "Signal processing for

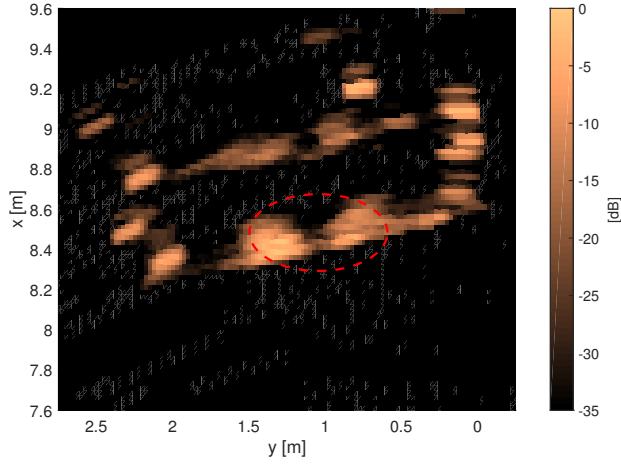


Fig. 21. Reconstructed image via CBP: 15 cm separation.

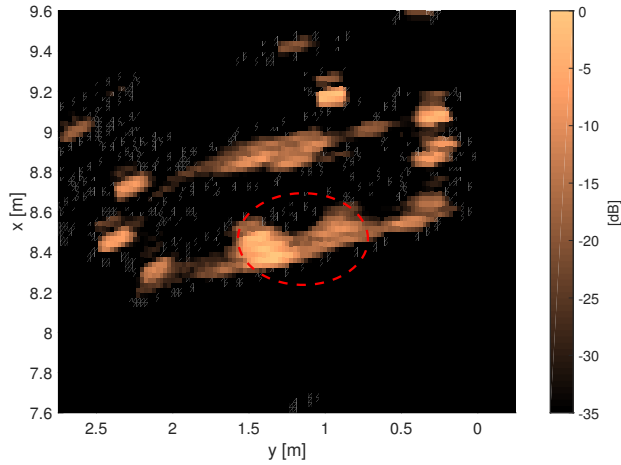


Fig. 22. Reconstructed image via CBP: 5 cm separation.

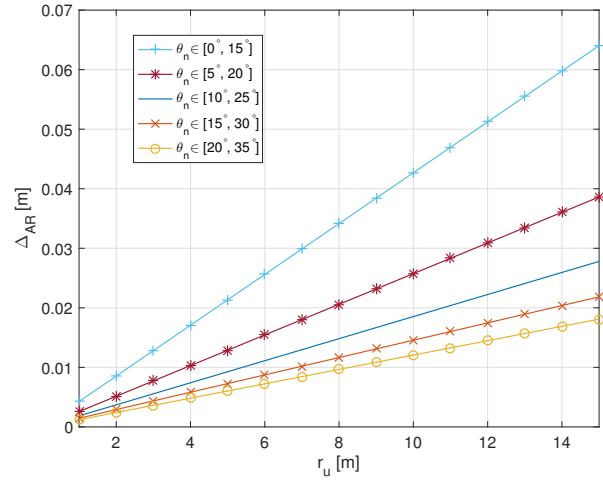


Fig. 23. Quantitative Analysis of FS-SAR (17).

- FMCW SAR," *IEEE Transactions on Geoscience and Remote Sensing*, vol. 45, no. 11, pp. 3519–3532, Nov 2007.
- [26] R. Wang, O. Loffeld, H. Nies, S. Knedlik, M. Hagelen, and H. Essen, "Focus FMCW SAR data using the wavenumber domain algorithm," *IEEE Transactions on Geoscience and Remote Sensing*, vol. 48, no. 4, pp. 2109–2118, April 2010.
- [27] A. Ribalta, "Time-domain reconstruction algorithms for FMCW-SAR," *IEEE Geoscience and Remote Sensing Letters*, vol. 8, no. 3, pp. 396–400, May 2011.
- [28] W. Carrara, R. Goodman, and R. Majewski, *Spotlight Synthetic Aperture Radar*. Boston: Artech House, 1995.
- [29] D. L. Donoho and M. Elad, "Optimally sparse representation in general (non-orthogonal) dictionaries via  $\ell_1$  minimization," *Proc. Natl Acad. Sci. USA*, vol. 100, no. 5, 2003, pp. 2197–2202.
- [30] E. Candes and T. Tao, "Decoding by linear programming," *IEEE Transactions on Information Theory*, vol. 51, no. 12, pp. 4203–4215, 2005.
- [31] E. Candes and M. Wakin, "An introduction to compressive sampling," *IEEE Signal Processing Magazine*, vol. 25, no. 2, pp. 21–30, 2008.
- [32] G. Hennenfent and F. J. Herrmann, "Simply denoise: Wavefield reconstruction via jittered undersampling," *GEOPHYSICS*, vol. 73, no. 3, pp. V19–V28, 2008.
- [33] R. Tibshirani, "Regression shrinkage and selection via the LASSO," *Journal of the Royal Statistical Society, Series B*, vol. 58, pp. 267–288, 1994.
- [34] R. Tibshirani, M. Saunders, S. Rosset, J. Zhu, and K. Knight, "Sparsity and smoothness via the fused LASSO," *Journal of the Royal Statistical Society Series B*, pp. 91–108, 2005.

- [35] D. P. Bertsekas and J. N. Tsitsiklis, *Parallel and Distributed Computation: Numerical Methods*, 1997.
- [36] S. Gishkori and G. Leus, "Compressed sensing for block-sparse smooth signals," in *IEEE International Conference on Acoustics, Speech and Signal Processing (ICASSP)*, May 2014, pp. 4166–4170.
- [37] A. F. Yegulalp, "Fast backprojection algorithm for synthetic aperture radar," in *Proceedings of the IEEE Radar Conference. Radar into the Next Millennium*, 1999, pp. 60–65.
- [38] L. M. H. Ulander, H. Hellsten, and G. Stenstrom, "Synthetic-aperture radar processing using fast factorized back-projection," *IEEE Transactions on Aerospace and Electronic Systems*, vol. 39, no. 3, pp. 760–776, July 2003.
- [39] P. O. Frolind and L. M. H. Ulander, "Evaluation of angular interpolation kernels in fast back-projection SAR processing," *IEEE Proceedings - Radar, Sonar and Navigation*, vol. 153, no. 3, pp. 243–249, June 2006.
- [40] A. Ribalta, "Optimizing the factorisation parameters in the fast factorized backprojection algorithm," in *9th European Conference on Synthetic Aperture Radar (EUSAR)*, April 2012, pp. 356–359.
- [41] M. Teichman, "Determination of horn antenna phase centers by edge diffraction theory," *IEEE Transactions on Aerospace and Electronic Systems*, vol. AES-9, no. 6, pp. 875–882, Nov 1973.
- [42] B. Efron and R. J. Tibshirani, *An Introduction to the Bootstrap*. New York: Chapman & Hall, 1993.



**Shahzad Gishkori** received the B.Sc. degree in electrical engineering in 2002 from the University of Engineering and Technology Lahore, Pakistan and later on worked in the industry for almost five years. He received the M.Sc. degree (cum Laude) and the Ph.D. degree in electrical engineering from the Delft University of Technology, The Netherlands, in 2009 and 2014, respectively. From 2014 to 2015, he was a postdoctoral research associate at Imperial College London, UK. Since February 2016, he has been working as a postdoctoral research associate at The University of Edinburgh, UK. His research interests include compressed sensing, signal processing and wireless communications.



radar systems.

**Liam Daniel** received the M.Sci. degree in Theoretical Physics in 2005 and his Ph.D. in Maritime Forward Scatter Radar Development in 2017, both from the University of Birmingham, Birmingham, U.K. He is currently a Research Fellow in the Microwave Integrated Systems Laboratory in the School of Engineering at the university. His research interests include experimental, theoretical, simulation and signal processing aspects of bistatic radars with a focus on forward scatter radar and passive sensing. Current work focusses on automotive sensing and low-THz



**Marina Gashinova** (MMath, 1991, PhD in Physics and Mathematics, St.-Petersburg, Russia, 2003). In 2006 she joined Microwave Integrated System Laboratory at the University of Birmingham, UK, as a Research Fellow, and now she is a Senior Lecturer in Radar and RF Sensors, leading the research group on passive and active bistatic radar, THz multi-feature imaging radar and automotive sensors.



**Bernard Mulgrew** (FIEEE, FREng, FRSE, FIET) received his B.Sc. degree in 1979 from Queen's University Belfast. After graduation, he worked for 4 years as a Development Engineer in the Radar Systems Department at Ferranti, Edinburgh. From 1983-1986 he was a research associate in the Department of Electrical Engineering at the University of Edinburgh. He was appointed to lectureship in 1986, received his Ph.D. in 1987, promoted to senior lecturer in 1994 and became a reader in 1996. The University of Edinburgh appointed him to a Personal Chair in October 1999 (Professor of Signals and Systems). His research interests are in adaptive signal processing and estimation theory and in their application to radar and sensor systems. Prof. Mulgrew is a co-author of three books on signal processing.